



## TELESCOPES AND INSTRUMENTATION

### ISAAC at the VLT

A. MOORWOOD, J.-G. CUBY, P. BALLESTER, P. BIEREICHEL, J. BRYNNEL, R. CONZELMANN, B. DELABRE, N. DEVILLARD, A. VAN DIJSSELDONK, G. FINGER, H. GEMPERLEIN, C. LIDMAN, T. HERLIN, G. HUSTER, J. KNUDSTRUP, J.-L. LIZON, H. MEHRGAN, M. MEYER, G. NICOLINI, A. SILBER, J. SPYROMILIO, J. STEGMEIER

ESO

#### 1. Introduction

ISAAC (Infrared Spectrometer and Array Camera) provides for 1–5  $\mu\text{m}$  imaging; 1–2.5  $\mu\text{m}$  polarimetry and 1–5  $\mu\text{m}$  spectroscopy and is the first VLT instrument fully developed by ESO. Figure 1 shows it mounted on the adapter/rotator at the Nasmyth B focus of the first of the four 8.2-m VLT Unit Telescopes. ISAAC itself is cryogenically cooled and housed within a 1.6-m diameter vacuum vessel enclosed by the red protective cover seen in this photograph. The large unit to the right, flanked by the two racks of control electronics, is the cable co-rotator system which carries the electrical cables and closed-cycle cooler hoses to the instrument and rotates with it as the telescope tracks objects on the sky. Following integration and extensive testing in Garching, ISAAC was delivered to the Paranal Observatory in June 1998 where it was re-assembled and re-tested in the Integration Laboratory prior to installation on the telescope, as scheduled, on November 14th. First light images were already shown in *The Messenger* 94, 7, and accompanied by a very short article written in the VLT control room while the



Figure 1: ISAAC installed at the Nasmyth B focus of the VLT UT1. The instrument, enclosed in its protective red cover, is attached to the adapter/rotator system at the left and has a total weight of around 1.5 tons. The box at the left contains some of the electronics required for controlling and reading the two infrared array detectors. To the right is the co-rotator system that transfers all the electrical cables and gas hoses for the closed-cycle coolers to the instrument and rotates with it and the adapter. At each side of the co-rotator are cabinets containing electronics for controlling and monitoring the instrument functions and the vacuum and cryogenic system. At the bottom can be seen part of the platform to which the instrument is attached for installation, removal and maintenance activities.



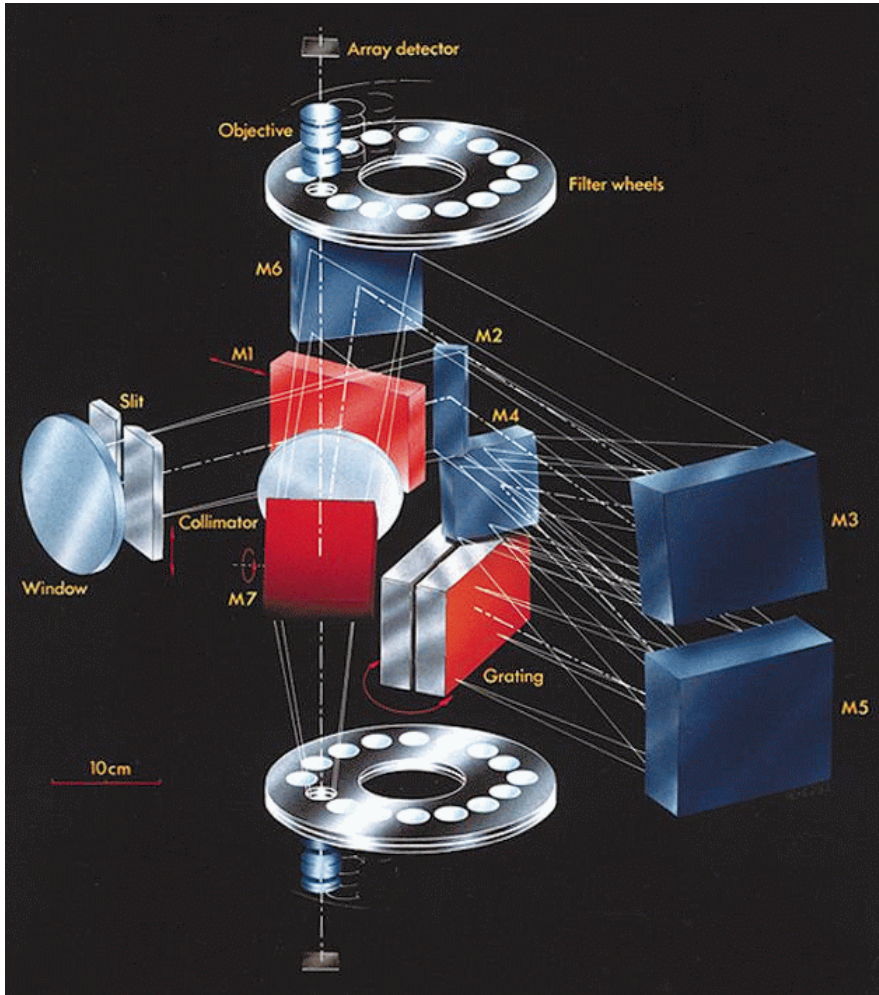


Figure 2: Optical layout of ISAAC. See text for a detailed explanation.

first tests were still in progress. Just prior to the planned start of routine operations on April 1st, it is appropriate here to briefly recall its design and development, report on its performance during the commissioning tests and present some spectra of relatively faint objects which illustrate further the new scientific capabilities now offered by this instrument.

## 2. Scientific Capabilities

Scientific interest in ISAAC encompasses most topics in modern astronomy from the study of faint outer solar-system bodies to the most distant galaxies and clusters. In these and other areas, such as the study of Brown Dwarfs and low-mass stars, its particular strength lies in the possibility of both making deep imaging observations and surveys and following them up spectroscopically. There is no space here to enter into a detailed discussion of the scientific results and discoveries to be expected. It is, however, interesting to recall that near-infrared imaging and spectroscopy of high redshift galaxies was highlighted in the original ISAAC Design and Implementation Plan of October 1991 as the area which could potentially gain most from such an instrument on a large telescope. More specific topics mentioned were the observation of 'visible' lines for redshift de-

terminations, deep searches for extremely red, possibly primeval galaxies, studies of cluster evolution, etc. Although apparently trivial as a prophecy now, few high  $z$  galaxies were actually known at that time and the enormous level of current activity and interest in this area together with the relatively large fraction of ISAAC observing time allocated to it in P 63 is therefore rather comforting. That the required sensitivity can actu-

Figure 3: ISAAC with its front vacuum flange removed revealing the slit/mask wheel and the casting used to support its various opto-mechanical functions, including the two cameras which are partly visible to the upper and lower right of the centre.



ally be reached is also supported by some of the spectra obtained during commissioning and shown here.

## 3. Observational Modes

ISAAC offers the following observational modes:

- Imaging through broad- and narrow-band filters
  - 0.9–2.5  $\mu\text{m}$  with a  $2.5 \times 2.5'$  field of view and 0.147" pixels
  - 2.5–5  $\mu\text{m}$  with a  $40 \times 40''$  max. field of view and pixels of 0.16" and 0.08"
- Imaging polarimetry
  - 0.9–2.5  $\mu\text{m}$  using a Wollaston prism with broad-band and a limited set of narrow-band filters
- Spectroscopy at  $R_s \sim 500$  and 3000 and slit widths of 0.3, 0.6, 1 and 2"
  - 0.9–2.5  $\mu\text{m}$  with a slit length of 2'
  - 2.5–5  $\mu\text{m}$  with a slit length of 40"

The more detailed information required for making an observing proposal can be found on the Web (<http://www.eso.org/observing/observing.html>).

## 4. Design and Development

Figure 2 shows the optical layout of ISAAC. It contains two cameras (each comprising 2 filter wheels, an objective wheel and an array detector) one of which is optimised for the 1–2.5  $\mu\text{m}$  and the other for the 2.5–5  $\mu\text{m}$  spectral ranges. For imaging and polarimetry the light entering the window at the left passes through the slit/mask wheel, is diverted by the mirror M1 through the 16-cm-diameter BaF<sub>2</sub> collimator/field lens and to the required camera by the M7 selector mirror. For spectroscopy the mirror M1 is retracted, allowing light from the slit to

pass through the spectrometer unit to form an intermediate spectrum close to M6 which is then re-imaged by the selected camera. The spectrometer unit consists of 2 back-to-back mounted gratings – for the low- and medium-resolution modes – and a mirror system comprising three hyperbolic mirrors (M3, M4, M5), which were diamond turned on nickel-coated aluminium and then hand post polished and gold coated. This system is used both to collimate the 10-cm-diameter beam and to form the intermediate spectrum after dispersion at the grating. Attached to the front of the instrument is the pre-slit unit containing a pupil lens, integrating sphere, continuum plus line lamps for flat fielding and wavelength calibration and a technical CCD for slit viewing.

The 1–2.5  $\mu\text{m}$  (SW) ‘arm’ is equipped with a  $1024 \times 1024$  pixel Hg:Cd:Te array manufactured by the Rockwell International Science Center and the 2.5–5  $\mu\text{m}$  ‘arm’ with a  $256 \times 256$  InSb array from the Santa Barbara Research Center. Detector control and data acquisition is via the ESO-developed high-speed IRACE system (Meyer et al. 1996).

Most of the moving functions in ISAAC (slit/mask wheel, M1 and M7 selector mirrors, grating, filter and objective wheels) are mounted on paired, angular contact, bearings and driven by 5-phase stepper motors (modified at ESO for cryogenic operation) and stainless steel worm gears acting on Vespel or Nylcast toothed wheels attached to the functions. The linear lens collimator drive employs a pre-loaded roller screw. Initialisation of the functions is by means of magnetic sensors. In the case of the bearings, the steel balls were replaced by tungsten carbide ones and the separators by self-lubricating Nylcast cages impregnated with 321R from Dow Corning. Because of the inherent difficulty in developing such high-precision moving functions for operation at cryogenic temperatures in vacuum, both the individual components as well as a complete prototype unit were extensively tested before the Final Design Review of the instrument. The various optomechanical functions, including their drive systems, are all supported by a cast aluminium structure surrounded by a radiation shield and attached to the vacuum vessel by two fibreglass ‘spiders’. Figure 3 shows ISAAC with the front cover of its vacuum vessel removed and provides a view of the cast structure plus the large slit/mask wheel and parts of the two cameras. Access to the spectrometer is by removing the rear vacuum flange. Total mass of the cryogenically cooled part is 350 kg. Despite this large mass, it can be cooled to its operating temperature of 70 K (and the detectors to as low as 25 K) in 24 hours using a liquid-nitrogen continuous-flow circuit during this phase to boost the cooling power of the two closed-cycle coolers used to maintain the required temperatures during normal operation. Evacuation is by means of a back-pump behind a turbomolecular pump



Figure 4: Colour composite image of the merging galaxy system ESO202-G23 which combines a 1200s ISAAC H (1.65  $\mu\text{m}$ ) band exposure with B (1800s) and R (900s) images obtained with the VLT test camera. The field shown here is  $\sim 1.5'$  with north at the top and east to the left and the seeing was  $\sim 0.4''$ . Visible are at least one Active Galaxy Nucleus with an associated ionisation cone; a blue star-forming complex to the south; and a complicated pattern of emission resulting from the merger and heavy extinction. Of additional interest is the arc of more distant red galaxies in the lower part of the image.

flanged directly onto the vacuum vessel. All cryogenic operations during cool-down and warm-up are controlled automatically by the control system which also monitors temperatures/pressure and sounds safety alarms and/or initiates safety features (e.g. automatic warming up of the detectors in case of loss of cooling power or a rapid pressure rise). Additional details of the design have been given by Moorwood (1996) and of the integration phase in Garching by Lizon (1996).

## 5. Performance

Based on the commissioning tests and observations made so far, the astronomical performance of ISAAC fully lives up to expectations. The combination of excellent telescope and instrument optical quality delivers fully seeing-limited images with a smallest FWHM so far of  $0.28''$ . The arrays are cosmetically good, the fields ‘clean’ and flat (to a few per cent before flat fielding), internal flexure is less

than 0.5 pixel and the limiting magnitudes are set by the sky + telescope background and the seeing. For observations in the thermal infrared, beyond 2.5  $\mu\text{m}$ , the telescope passed with flying colours its most difficult challenge of performing the active optics corrections while nodding plus chopping and field stabilising with M2.

Given the new maturity of infrared capabilities, it is likely that many scientific programmes will increasingly combine visible and infrared data. As an example, Figure 4 shows a colour composite (B, R, H(1.65  $\mu\text{m}$ )) image of the merging active galaxy system ESO202-G23 made by combining images obtained with ISAAC and the VLT test camera and which adds to the diagnostic power of the visible or infrared images alone. A selection of other illustrative images has already been presented in *The Messenger* 94, 7 (1998) and on the Web (<http://www.eso.org/outreach/press-rel>).

Low-resolution spectroscopy at most wavelengths is also background limited by the radiation from the sky and tele-



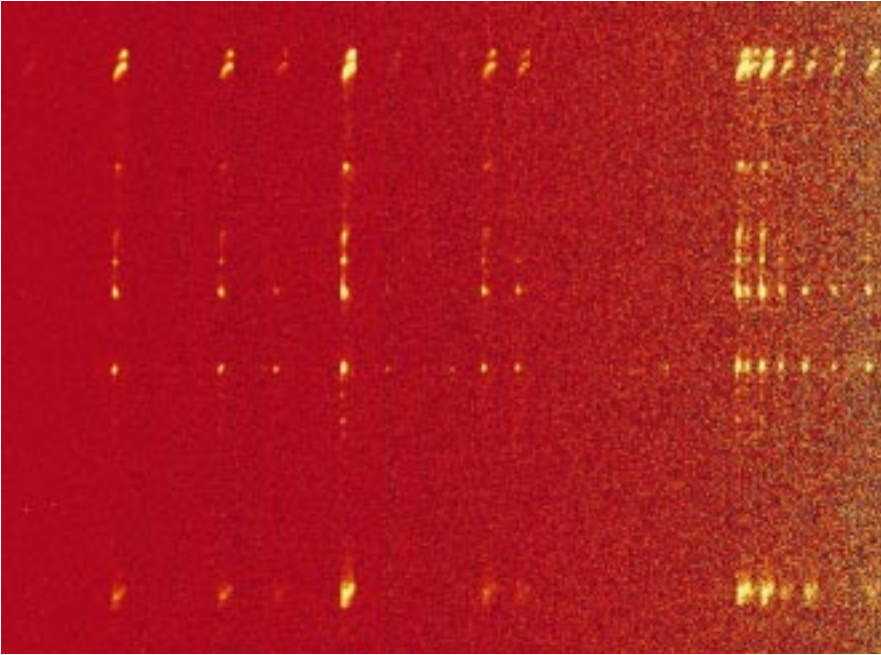


Figure 5: Low-resolution 2–2.5  $\mu\text{m}$  spectral image of HH212 which fully exploits the 2' long slit. This galactic object is believed to harbour a heavily obscured protostar that has expelled material periodically during its evolution. What is remarkable is the degree of symmetry of the 'bullets' ejected in opposite directions. Each of the 'images' seen here corresponds to a different emission line of interstellar molecular hydrogen that has been excited by the impact of the ejected material.

scope. Examples are shown in Figures 5 and 6 which show a K band spectral image of the fascinating Herbig Haro object HH212 and J, H, K band spectra of the radio galaxy MRC0406-244 plus two ex-

tremely red, nearby, galaxies. At medium resolution ( $R \sim 3000$ ) in the J and H bands, however, regions between the OH sky lines open up where the background continuum has been measured to be ex-

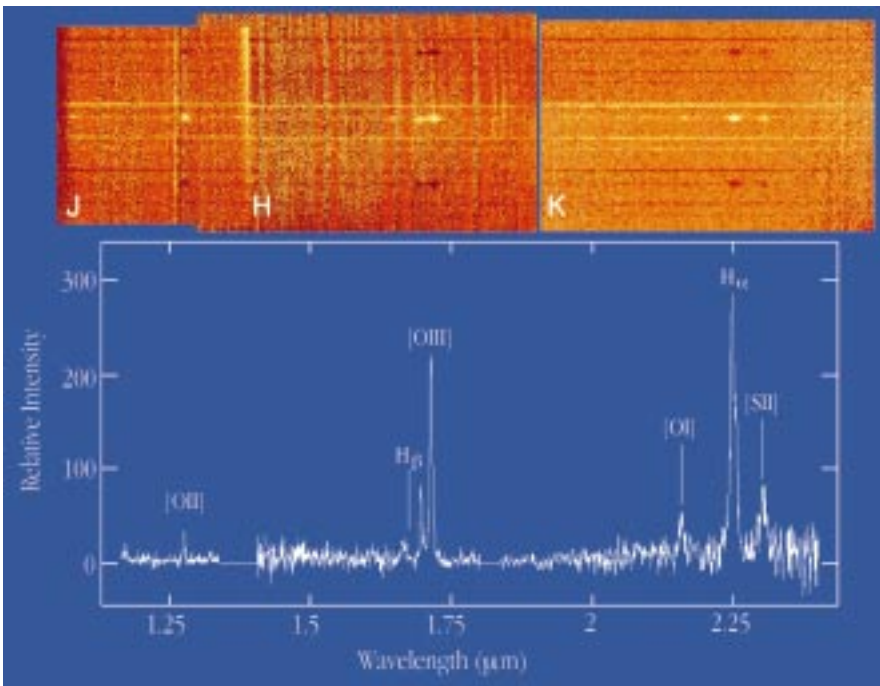


Figure 6: The upper panel shows a montage of low-resolution ( $R \sim 500$ ) spectral images covering most of the 1–2.5  $\mu\text{m}$  region of the  $z = 2.4$  radio galaxy MRC0406–244 plus two extremely red ( $R-K > 5$ ) galaxies below and an anonymous one above. Integration times were 2 hours in the J and 1 hour in H and K bands. The negative images of the spectra result from the technique used for sky subtraction, and the vertical stripes are due to increased photon shot noise at the positions of OH night sky lines. The extracted spectrum of the radio galaxy in the lower panel shows the prominent, redshifted, emission lines [OII],  $H\beta$ , [OIII] (doublet), [OI],  $H\alpha$  and [SII] (doublet) normally observed at visible wavelengths in nearby objects. The apparent absence of these lines in the spectra of the companion red galaxies casts some doubt on the suggested possibility that they are members of a cluster at the same redshift as the radio galaxy.

tremely low ( $< 0.1 \text{ e}^-/\text{s}$ ). As the detector dark current is even lower than this, sensitivity in these regions is limited essentially by the detector read noise ( $< 10 \text{ e}^-$ ), bad pixels and cosmic rays. This is illustrated by Figure 7 which shows medium-resolution spectra around 1.06  $\mu\text{m}$  of redshifted  $H\alpha$  (+[NII]) emission in two  $z \sim 0.62$  galaxies from the CFRS catalogue which are only a few arcsec apart on the sky (Hammer et al. 1995). Finally, Figure 8 shows an example of medium-resolution 'imaging' spectroscopy in the form of a spectrum of SN 1987A obtained through the 2" slit and with the grating set close to the He I 1.083  $\mu\text{m}$  line.

Because performance is a strong function of mode, wavelength, conditions, etc, it is difficult, and potentially misleading, to summarise it in a few numbers here. The information is available, however, and has been incorporated into the ISAAC Exposure Time Calculators, the ISAAC Users Manual and other information which is available and will be maintained on the Web (<http://www.eso.org/observing/observing.html>).

## 6. Observing with ISAAC

Routine observations with ISAAC are planned to start in P 63 on April 1st, 1999. Of course, ISAAC is fully embedded in the VLT operational philosophy and data-flow system as described in detail on the Web (<http://www.eso.org/org/dmd>). The normal starting point in preparing proposals will probably be to consult the Instrument Description, Users Manual, etc. on the Web and to use the Exposure Time Calculators (ETC) referred to above to assess feasibility and estimate the required integration times. Proposals can then be submitted for either Service or Visitor Mode observations as described in ESO's Announcement for the relevant period. In both cases, the actual observations will be executed at the telescope via Observing Blocks consisting of acquisition and instrument (observation description) templates, which set the various, instrument functions and parameters and control the exposures via a sequencer. Real time feedback on the instrument status and the progress of the observations is provided via the Observing Software display on the instrument workstation and the actual images are displayed on a Real Time Display (RTD). The RTD is also used interactively in some modes e.g. to 'drag' objects seen in the imaging mode into the slit for spectroscopy and to determine pixel values, coordinates, image quality, etc. All raw data are archived as are those reduced by the reduction pipelines whose current status is described separately by Devillard et al. in this issue. Additional observations defined in a Calibration Plan will also be conducted by ESO in order to maintain the instrument performance, analyse trends (e.g. in zero point, dark and flat field variations) and to allow calibration of Service Mode data to a specified level.

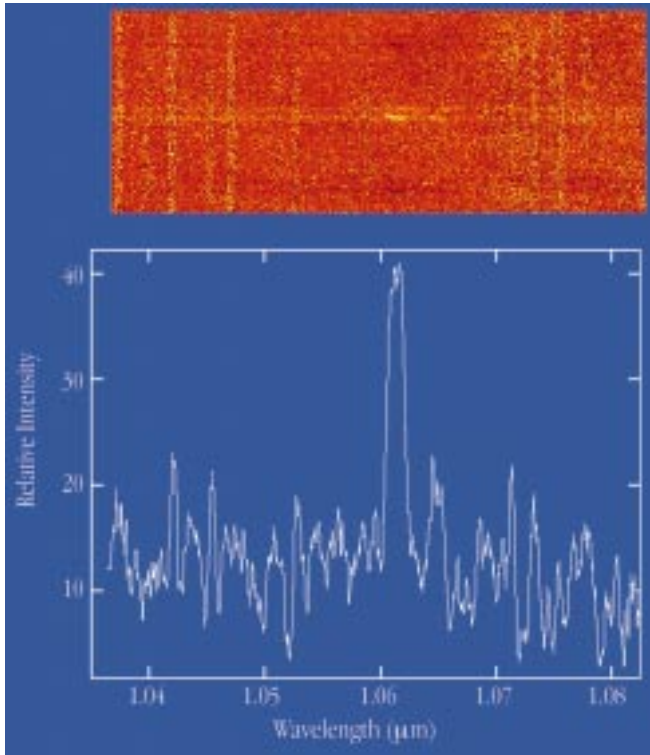


Figure 7: The upper panel shows a medium resolution ( $R \sim 3000$ ) spectral image around  $1.06 \mu\text{m}$  of two galaxies at  $z \sim 0.62$  selected from the CFRS catalogue. Total exposure time was 1 hour. The lower panel shows the extracted spectrum of the brighter galaxy which, in addition to the continuum, shows bright redshifted  $H\alpha$  and fainter [NII] (to the right) emission lines. As can be seen in the image, the  $H\alpha$  emission appears to be tilted relative to the continuum due to the rotation of the galaxy which can thus be measured to provide an estimate of its mass.

## 7. Acknowledgements

We wish to particularly thank the ISAAC Science Team R. Chini, G. Miley, E. Oliva and J.-L. Puget for their suggestions and encouragement throughout the design and development phase; R. Gilmozzi, P. Gray, M. Petr, G. Rahmer and P. Sans-

gasset for their support during installation and commissioning on Paranal and J. Alves, P. Amico and M. Kissler-Patig in Garching. Collective thanks are also due to many other people, too numerous to mention individually and within all Divisions of ESO, who have contributed to this project. We are also grateful to L.

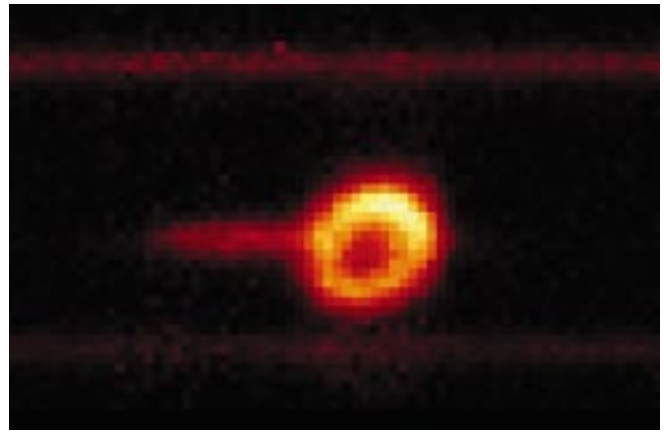


Figure 8: A spectral image of SN 1987A in the  $\text{HeI}$  ( $1.083 \mu\text{m}$ ) line obtained in a 20-min exposure using the medium-resolution grating and a  $2''$  wide slit. The ring is formed of gas blown off the progenitor star during its evolution and which was first photoionised by UV light from the SN and more recently shock ionised by ejecta which, travelling at  $30,000 \text{ km/s}$ , has only just reached it after a travel time of nearly 12 years. The jet-like feature extending to the left is actually in the spectral dispersion direction and shows the presence of a blue-shifted, high-velocity component that is believed to arise in the ionised ejecta.

Tresse and O. Le Fèvre for detailed information on the CFRS galaxy sample.

## References

- Hammer, F., Crampton, D., Le Fèvre, O., Lilly, S.J. 1995, *ApJ*, **455**,88.  
 Lizon, J.-L. 1996, *The Messenger*, **86**, 11.  
 Meyer, M., Finger, G., Mehrgan, H., Stegmeier, J., Moorwood, A.F.M.: 1996, *The Messenger*, **86**, 14.  
 Moorwood, A.F.M. 1996, In *Optical Telescopes of Today and Tomorrow* (ed. A. Ardeberg), *SPIE* Vol. 2871, 1146.

amoor@eso.org

# ISAAC Pipeline Data Reduction

N. DEVILLARD, Y. JUNG, J.-G. CUBY, ESO

The ISAAC pipeline, just as the pipeline for any other VLT instrument, is built to provide reduced data on site in order to assess their quality as soon as possible. Another version of the same software will also be running in Garching for quality control, trend analysis, and service-observing data-reduction purposes. All instrument pipelines share the same generic structure, taking care of data handling, i.e. transfers and reduction recipe triggering. The recipes themselves are specific to each instrument, they are plug-ins hooked into this generic data-handling structure, and they can be described as specialised tasks attached to an instrument-acquisition template. For more details about pipelines and Data Flow, the reader is referred to the ESO Web pages

and corresponding reference documents.

The following instrumental modes are supported in pipeline mode for the first ISAAC period: imaging jitter, twilight flat, darks and bad pixel map creation, illumination frames and zero-point computations. In spectroscopy: NodOnSlit, flat-field, spectroscopic response function, star trace calibration, and slit position. We give here an overview of the algorithms used to reduce the data without user intervention for all these modes, so that observers can get a rough idea of what is done in pipeline mode, what the working domain for the recipes is, what can be obtained in the control-room at runtime, and how to reproduce these reduction processes at their home institute if they wish to.

## 1. Imaging Mode

Imaging recipes (procedures) are based on the ESO **eclipse** library, mainly to speed up the number-crunching process (see article in *The Messenger* No. 87, p. 19–20). The eclipse library is exportable, compiles on virtually any (recent) Unix machine that has minimum POSIX compatibility, and is available on the Web at the following address: <http://www.eso.org/eclipse/>

### Calibration recipes

Dark frames are acquired through a dedicated template, which stores several dark frames for each possible DIT (Detector Integration Time), and usually



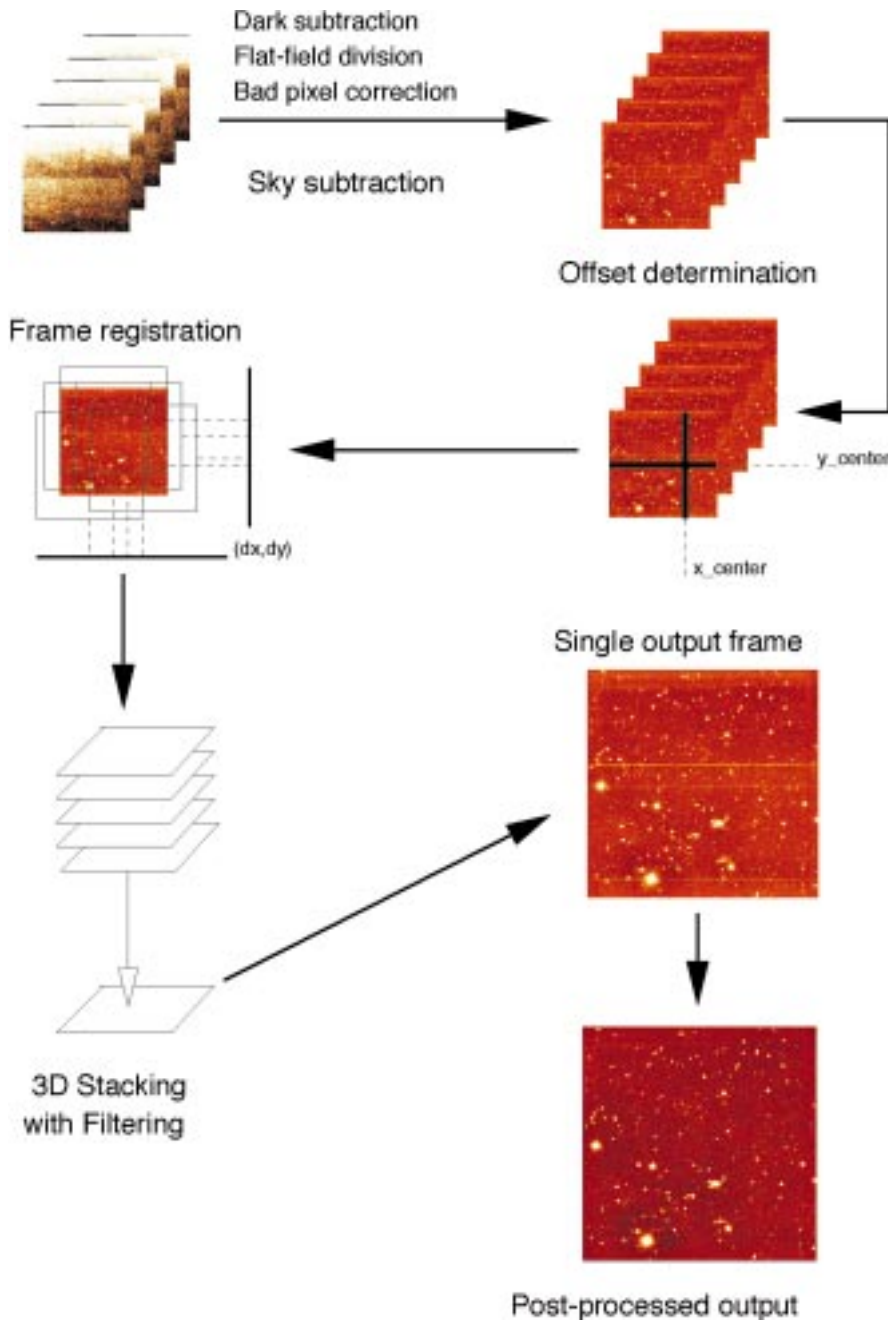


Figure 1.

covers several DIT values. The output of this template is a list of frames containing dark exposures, which need to be sorted out by DIT group and then averaged per group with rejection criteria to avoid cosmics. The output of the **is\_darks** procedure is a list of frames, one for each given DIT. Read-out noise is also measured from these frames and the information is written to a readable ASCII file. The associated eclipse routine is **is\_darks**. It is recommended to take 5 darks or more per DIT you used during the observation night, so that the computed master dark frame is reasonably reliable.

Twilight flatfields are acquired through a template that observes the sky at dawn or dusk with a constant integration time. Produced frames have an increasing or decreasing signal value that is used to measure detector linearity. For each pixel on the detector, a curve is plotted of the

median plane value (x axis) against the individual pixel value in this plane (y axis). This curve shows the pixel's response, from which a robust linear regression provides a pixel gain. The image showing all pixel gains (i.e. the flatfield) is normalised to have an average value of 1. Some criteria can be added later to check that the pixel behaviour is indeed linear, and build a bad pixel map for pixels that have excessively high or low gains, or do not behave linearly at all. The same procedure could be used with any kind of increasing/decreasing signal, which allows to sample the pixels' response at various points. The associated eclipse routine is called **flat**.

Flat-fields are usually corrected for low-frequency variations which are not taken into account by the twilight flat procedure. To compute these variations, a dedicated calibration template is offered. The procedure images a standard star on a grid

of  $4 \times 4$  or  $5 \times 5$  positions, with the convention that the first acquired frame shall contain the standard at the centre of the image, and subsequent positions be indicated through keywords in the FITS header. Photometry is computed for each star position and a 2d second-degree polynomial is fitted through the obtained surface. An image is generated from this polynomial with an average value of 1. The associated eclipse routine is **is\_illum**.

Zero-point acquisitions are done by observing a standard star with wide offsets on the detector. The operator at the instrument is in charge of locating the standard star through finding charts and positioning it at the centre of the array for the very first frame. Subsequent frame offsets are indicated in the FITS header. The recipe identifies the exact position of the standard star up to  $\pm 50$  pixels from the centre, computes the number of counts, and relates that measurement to a standard star database. The possible telescope pointing errors are not relevant to this case, because the star has been identified and positioned by human means. This is necessary to ensure that the star is actually in all frames and this is part of the acquisition process for this template. As a consequence, the algorithm does not need automatic astrometric calibration but a simple local peak-finder method. The ideal would be to provide star localisation through un-supervised astrometry; this may be implemented later. The identified infrared star database at this moment contains about 800 star positions with magnitudes in bands J, H, K, Ks, L, M. Some stars have missing information, it is recommended to test out beforehand that the standard star you will be using can actually be found and used from this database. The star search only looks for the closest star in position from RA and DEC information in the header, and computes zero-point information from it. In case of star mismatch (e.g. several standards are in the field), it should be easy to check out that the star used corresponds to the acquired one because all data relative to the used star are given along with the measured values. The standard star database is currently accessible through an eclipse command called **std**. Later on, access should be given through the Web to this list and users should be able to provide their own standards. The associated eclipse routine for zero-point computation is called **is\_zerop**. Notice that this method will not apply to standard stars in crowded fields, since it is relying on the assumption that the standard star to look for is the brightest object in the centre of the first frame, a condition that is not fulfilled in that case.

### Observation recipes

The main instrumental mode supported by the pipeline is the jittering mode (also known as microscanning). In this mode, no direct sky observation is performed, which maximises observation efficiency. However, a number of as-

sumptions must be fulfilled in order to use this template. The observation procedure is to first centre the first frame on the target, then acquire images with small telescope offsets between frames. The offsets requested to the telescope are stored along in the FITS headers. Of course, the usable part of the data seen through the detector is the intersection of all frames so the offsets should not be too large. On the other hand, the very aim of these offsets is to show what the sky background is to the detector, so offsets should be larger than the largest object on the frame. This means that the method can only be used with relatively small objects, which is typically the case for deep fields. For extended objects or crowded fields, the option is to apply this jittering to two positions: one on the target and another one on an empty field anywhere nearby, the immediate result being a loss of observing efficiency without which no sky subtraction is possible. In this case, we are talking about a jitter+offset mode. The idea in that case is to use the jittered pattern on the (empty) sky frames to filter out all possible remaining object signals and produce a clear sky that is subtracted from object frames. For the moment, the method running in the pipeline is taking a median average of all sky frames and subtracting it from the objects, but that would only work for small numbers of frames. Later implementations will offer various sky filtering algorithms depending on the actual acquisition duration and filter used.

In pure jitter mode (all frames acquired on the object), the instrument has a built-in offset generation method that scatters points optimally with a Poisson distribution law. The generated offsets have the property to be optimally distributed over the possible range of offsets, and thus maximise the chances of being able to filter out the sky background (see the `poisson` command in eclipse). It is recommended to use the `AutoJitter` template unless you have specific needs for the offset values and provide your own to the `GenericOffset` template. Please note that this generic template cannot yet be supported in pipeline mode, because it leaves too many choices to the user to be able to support all possibilities. When we get experience about what is usually requested, some more reduction modes will be implemented for the most usual cases.

The reduction procedure for the jitter algorithm is shown in Figure 1. Pre-processing is done by applying dark subtraction, flatfield division, and bad-pixel correction if these calibration frames are available. The first algorithm step is then to filter out the sky background from raw images. This is done with a 3d-filter with pixel rejection, actually similar to the `imcombine` routine in IRAF. Sky statistics are accumulated at that point and written to an ASCII result file; they should be appended to the output file FITS header in later versions. The second step is to detect the offsets between frames. We

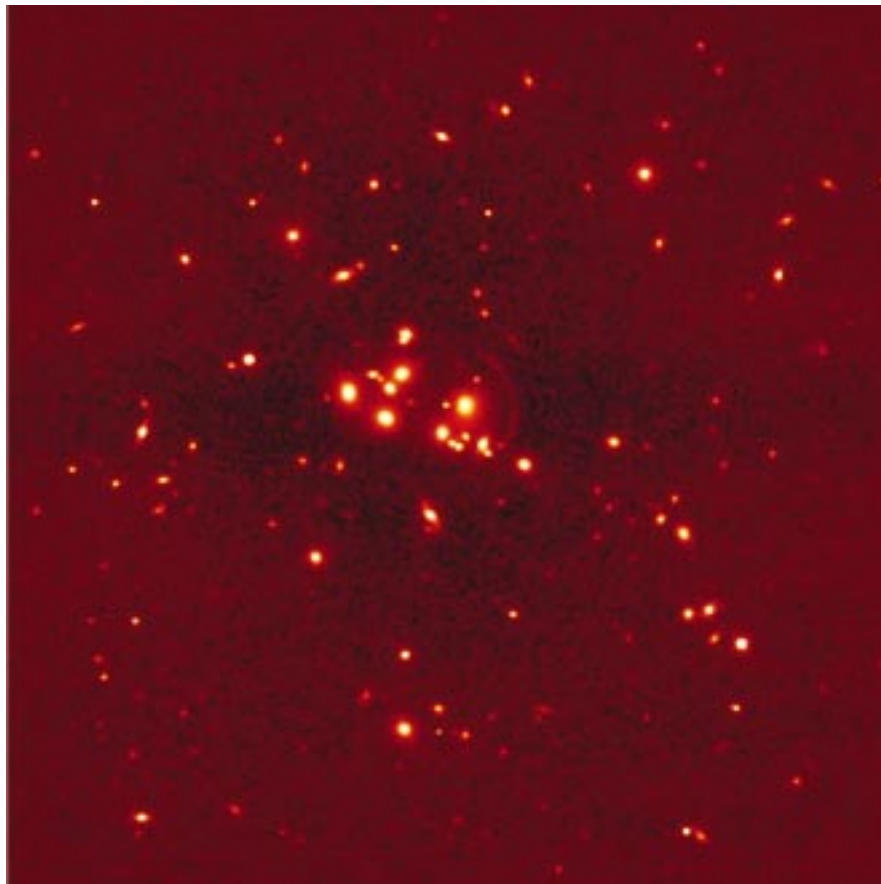


Figure 2.

need some useful signal in the frames to do that, and the best configuration is to be able to find the same bright object in all consecutive frames. If this is not possible, the algorithm would look for all bright objects it can find and try to locate them image after image, with sub-pixel precision. This is done through cross-correlation methods and is usually quite robust and insensitive to noise. The third step is to register all images to the first image taken as a reference. This is done through re-sampling methods in image space, and produces much less aliasing than Fourier space-based methods, linear interpolation, or just integer pixel moves. The only visible consequence is that noise (high frequencies) is smoothed out by the re-sampling process, but photometry is conserved. Once this is done, the last step is to stack all frames to a single one, using again a 3d-filter to remove spurious values. Post-processing is applied to this image to remove detector row saturation effects for example, then the result may be sent to an image displayer.

Figure 2 shows an image produced in November 1998 with ISAAC, the Galaxy cluster CL2244-02 with gravitational arcs (see press release dated 26 November 1998 on the ESO web site, and the December 1998 *Messenger* issue). This image is the jittered combination of 60 input frames in Ks band; it was obtained with default settings for all parameters. This is a typical output from the ISAAC pipeline in the control-room, for that kind of data.

This algorithm proves to be very reli-

able and usually complete for typical fields acquired so far with SOFI or ISAAC. There are still some incorrectly processed cases though, mostly for images where all bright objects are located on the edges of the first frame (the reference), but that should be solved with e.g. point-pattern matching algorithms in later releases of the pipeline. For more detailed information about the algorithm and what can be fine-tuned, readers are referred to the following document: "jitter imaging data reduction: algorithms and implementation".

The URL is <http://www.eso.org/projects/dfs/papers/jitter98/>

The software running automatically on both SOFI and ISAAC pipelines takes about 25 minutes (on a fast workstation with large amounts of memory) to reduce a batch of 60 frames, i.e. roughly 250 megs of data in input, and can run on virtually any POSIX-compatible machine. Supported OS's so far are Solaris, HP-UX, Linux, IRIX, AIX, DEC OSF/1, and any station that offers POSIX compatibility and an ANSI C compiler.

## 2. Spectroscopy Mode

The spectroscopy pipeline is made of MIDAS procedures making use of the LONG and ECHELLE packages, with some calls to eclipse routines to speed up pure image processing routines, and to perform standard star database search. It is likely that we will redevelop in C identified parts of the algorithm that are not likely to change and need CPU speed.

## Calibrations

Various calibration procedures are performed for trend analysis purposes; they are mainly used by the instrument scientist. They include a control of the slit position with respect to the detector, calibration of the spectroscopic dispersion relation with calibration lamps, analysis of known spectral lines to correct for spectrum tilts or curvature in the spatial direction, and spectroscopic flat-fields.

## Observations

Spectroscopic observations performed with the *NodOnSlit* template produce spectra on two different positions A and B obtained by a shift of the telescope along the slit. Each set of images is averaged to a single image, and both sets are subtracted from each other. Available outputs are images of (A-B), (B-A), and a combined image of those two. The com-

bined image is actually the most important one for the observer, since extraction will take place on this 2d-spectrum image. The pipeline goes on from this point, extracting the brightest spectrum from this image, performs flux and wavelength calibrations when adequate calibration data are available, and outputs the results to a FITS table.

The brightest spectrum is to be seen as a checkpoint: since it is usually a reference object, it might be useful to check out that the acquisition actually performed as expected at least on this object. This spectrum is available to the user in the control room, together with the combined 2d image so that spectrum extraction can proceed from that point (partly) by hand.

Notice that spectroscopy recipes should be distributed as a part of MIDAS in a subset dedicated to pipeline routines. Some are supporting an interactive mode that actually allows giving more indica-

tions about how the procedure runs and lead them to proceed directly to the solution for the spectra of interest.

## Acknowledgements

All ISAAC pipeline data reduction algorithms are based on the ISAAC calibration plan (ESO document VLT-PLA-ESO-14100-1384) by Pierre-Alain Duc and Jean-Gabriel Cuby. All procedures have been improved tremendously following the advice from Chris Lidman. Numerous discussions with Alan Moorwood, Almudena Prieto, Paola Amico, Pascal Ballester have helped a lot to clarify the requirements and improve the spectroscopy parts. The jitter process has received constructive and helpful comments from too many people to quote them all here; we thank them for their contributions.

ndevil@eso.org

# Commissioning FEROS, the New High-resolution Spectrograph at La Silla

A. KAUFER, O. STAHL, S. TUBBESING, Landessternwarte Heidelberg-Königstuhl  
P. NØRREGAARD, Astronomical Observatory Copenhagen  
G. AVILA, P. FRANCOIS, L. PASQUINI, A. PIZZELLA, ESO

## Introduction

On November 30, 1998, the second commissioning phase of the new Fiberfed Extended Range Optical Spectrograph (FEROS) was completed at the ESO 1.52-m telescope at La Silla.

The instrument had been installed by a small team from the Heidelberg, Copenhagen and La Silla observatories starting in mid-September – just two years after the contract signature between the FEROS consortium and ESO. FEROS saw its first stellar light at the end of the installation phase on October 6th.

An overview of the design and of the expected capabilities of the FEROS instrument has been presented in a previous paper [Kaufer et al., 1997, *The Messenger* 89, 1]; a more detailed description of the opto-mechanical design is found in [Kaufer & Pasquini, 1998, Proc. SPIE Vol. 3355, p. 844]. In the present article, the major technical results from the two commissioning phases which followed the first light event are reported.

## The Spectrograph Environment

Figure 1 shows the FEROS spectrograph inside its temperature and humidity controlled room, which was erected by the La Silla infrastructure team at the place of the former Echelec spectrograph inside the coudé room of the ESO 1.52-m telescope. The feet of the optical

bench are sitting on a platform coupled to the telescope pier but decoupled from the room's floor. The LN<sub>2</sub> supply tank is located outside of the spectrograph room in the neighbouring FEROS maintenance room and can be replaced every two weeks without entering the spectrograph room. Adding to these facts the very stable temperature which is maintained inside the room ( $\Delta T < 0.2$  K over 1 night), FEROS is located in a very stable environment – a crucial prerequisite for a long-term stability of the instrument as required for high-precision spectroscopic measurements.

From the spectrograph, the two fibers together with their metallic protection cable are led through the telescope's polar and declination axes, further inside the telescope's double tube, and eventually leave the telescope and enter the Boller & Chivens (B&C) Cassegrain spectro-

graph to end in the telescope's focal plane, which now hosts the new FEROS fiber head and the previous B&C long slit.

## Instrument Performance

Table 1 summarises some of the main performances of FEROS as determined during the commissioning.

## Efficiency

The detection efficiency of the complete system ESO 1.52-m telescope + fiber link + FEROS + Detector has been measured several times under photometric conditions using bright and faint CTIO standard stars [Hamuy et al., 1994, *PASP*, 106, 566]. Correction for the atmospheric extinction has been made according to the standard La Silla extinction tables. The typically achieved detection

Table 1: Measured performance of FEROS.

Wavelength Range in one exposure (object+sky)	360 – 920 nm (39 orders, 2 fibers)
Resolving Power	$\lambda/\Delta\lambda = 48,000$ (2.2 pixels)
Entrance Aperture	2.7 arcsec (circular)
Detection Efficiency (with telescope and detector)	1% at 360 nm, 16% at 440 nm, 17% at 550 nm 16% at 640 nm, 11% at 790 nm
Limiting Magnitudes at the ESO 1.52	16 mag in V, S/N = 9, $t_{\text{exp}} = 2$ h 12 mag in V, S/N = 105, $t_{\text{exp}} = 2$ h
Radial-Velocity Accuracy	21 m/s rms (2-month time base)
Inter-order straylight	< 3%